ARTICLE IN PRESS

Acta Biomaterialia xxx (xxxx) xxx

Contents lists available at ScienceDirect

Acta Biomaterialia

journal homepage: www.elsevier.com/locate/actbio

Full length article

Local mechanobiological disruption in solid tumor-driven vascular permeability: A competition between mechanical vs chemical stimuli

Alejandro Martín-Contreras [a], María Sarasquete-Martínez [b], José Manuel García-Aznar [a], Alejandra González-Loyola [a,c,d,1,*], María José Gómez-Benito [a,1,*]

[a] Department of Mechanical Engineering, Multiscale in Mechanical and Biological Engineering (M2BE), Aragon Institute of Engineering Research (I3A), University of Zaragoza, Zaragoza, Spain
[b] Department of Electrical Engineering and Communications, Biomedical Signal Interpretation and Computational Simulation (BSICoS), I3A, University of Zaragoza, Zaragoza, Spain
[c] Aragon Health Research Institute (IIS Aragón), Zaragoza, Spain
[d] Aragonese Agency Foundation for Research and Development (ARAID), Zaragoza, Spain

ARTICLE INFO

Keywords:
Vascular dysfunction
Mechanobiology
Endothelial barrier
Vessel-on-a-chip
Tumor microenvironment

ABSTRACT

The tumor microenvironment imposes complex biochemical and biomechanical constraints on microvasculature, contributing to aberrant tumor blood vessels, characterized by abnormal endothelial proliferation, disrupted cell-to-cell junctions and increased permeability. While vascular normalization strategies have traditionally focused on biochemical modulation, the role of mechanical forces in endothelial dysfunction remains unclear. Here, we used a microfluidic platform to dissect the mechanobiological impact of two distinct solid tumor models —pancreatic ductal adenocarcinoma (PANC-1) and lung adenocarcinoma (A549)—on three-dimensional embedded endothelial vessels. Our findings reveal that PANC-1 spheroids exert significant mechanical forces, expanding vessel diameter and disrupting endothelial barrier integrity via cellular contractility. Conversely, A549 spheroids contribute to vascular destabilization through biochemical modulation, primarily via extracellular matrix degradation and inflammatory secretomes, leading to an altered and heterogeneous endothelial permeability. Proteomic analysis of both tumor cell lines highlights distinct pathways involved in endothelial remodeling: cytoskeletal alterations and consequent stresses in pancreatic ductal adenocarcinoma, while extracellular matrix remodeling and pro-inflammatory microenvironment are found in lung adenocarcinoma. These insights underscore the necessity of tumor-specific vascular normalization strategies, combining mechanobiological and biochemical approaches to restore endothelial barrier function. Our locally controlled microfluidic approach provides a versatile platform for evaluating innovative therapeutic strategies targeting tumor-specific vasculature.

Statement of significance: This study highlights the often-overlooked role of tumor-derived mechanical forces in vascular dysfunction. Within the tumor microenvironment, different tumor types disrupt the endothelial barrier through distinct, tumor-specific mechanisms, leading to varied patterns of vessel instability. Using confocal microscopy, we achieved spatially resolved analysis of local endothelial barrier damage, distinguishing focal from diffuse permeability changes. A 3D microfluidic platform was developed to replicate tumor endothelium interactions, combining live imaging, morphometric and biochemical assays, and proteomic profiling. This integrative model offers a versatile tool for evaluating drug responses under controlled mechanochemical conditions, supporting the development of personalized vascular-targeted therapies.

1. Introduction

Solid tumor progression involves complex interactions within the tumor microenvironment (TME), a niche composed of cellular and non-cellular components that shift from an anti- towards a pro-tumoral landscape [1–4]. These alterations transform fibroblasts into CAFs,

---

* Corresponding authors.
E-mail addresses: agonzalezlo@iisaragon.es (A. González-Loyola), gomezmj@unizar.es (M.J. Gómez-Benito).
[1] Authorship note: they contributed equally to this work.

https://doi.org/10.1016/j.actbio.2026.01.013
Received 27 June 2025; Received in revised form 24 December 2025; Accepted 7 January 2026
Available online 8 January 2026

Please cite this article as: Alejandro Martín-Contreras et al., *Acta Biomaterialia,* https://doi.org/10.1016/j.actbio.2026.01.013

hamper the immune response, promote abnormal angiogenesis [4–7] and induce changes in the extracellular matrix (ECM) increasing its stiffness and reducing its porosity [8].

Among the TME components, the tumor microvasculature is particularly affected, exhibiting disorganized blood endothelial cell (BEC) proliferation, disrupted junctions and lack of pericyte and basal membrane coverage [9–11]. This results in increased vascular permeability, interstitial fluid pressure (IFP) and tumor hypoxia [12].

Mechanical stresses – arising from ECM stiffening and tumor expansion within a confined space [13,14] —are key contributors to endothelial dysfunction, hindering its function and facilitating tumor dissemination. These mechanical stimuli increase BECs' sensitivity to angiogenic factors, leading to dysfunctional vessels [15,16]. Also, increased IFP and the shear stress on the blood vessel wall and across the TME hinder BEC's functionality too [12]. Taking this vascular dysfunction into account, it has been described in the literature a strong coupling between vascular and interstitial flow, revealing a non-uniform IFP distribution. This is a result of the interplay between the blood flow in the vessels and the movement of the fluid in the interstitium [17]. There is a correlation between necrotic core size of tumors and IFP minimum values, with important implications for drug transport. The presence of lower pressure at the tumor core drive drug delivery towards these hypoxic regions, hindering its efficacy [17]. Normalizing vascular networks could enhance treatment efficacy by promoting drug perfusion and increasing drug residence time into the affected areas [18,19].

Because of this, vascular normalization has emerged as a key strategy to restore the microvasculature's functionality and increase efficacy of main therapies [9]. While anti-VEGF and Ang-2 therapies aim to normalize tumor vessels, they often fail to restore full functionality and may induce resistance or secondary hypoxia [18,20,21]. Mechanobiological strategies targeting ECM mechanics and fluid forces may better support vascular normalization and drug delivery [9,21].

Given the limitations of current models in capturing these biomechanical influences, microfluidic systems have emerged as powerful tools to dissect the role of mechanical constraints on vascular function with spatial and temporal resolution [22,23]. Vessel-on-a-chip platforms integrate 3D structures, ECM and several cellular populations, resulting in a better reconstruction of the stromal microenvironment and, consequently, in promising models to study the fluid dynamics of the vessel-TME interface [24–28]. Several microfluidic approaches have demonstrated the role of biomechanical environment in vessel permeability, tumor growth and drug transport [12,29–31]. Moreover, some studies have used different 3D vessels-on-a-chip platforms to study several processes affecting vessel permeability and barrier integrity, showing that permeability of BECs' vessels is increased in presence of tumor spheroids [32–34]. However, few research has analyzed local permeability associating mechanical loads exerted by tumor spheroids over the matrix and endothelial barrier integrity.

Despite the growing recognition of tumor mechanobiology, experimental models that allow for precise manipulation of mechanical constraints remain scarce. In this work, we present a 3D microfluidic model that simulates, in a precise and controlled way, the interaction between tumor spheroids and an embedded endothelial vessel. Unlike previous studies, our model allows to correlate local tumor spheroid-driven alterations in the surrounding ECM with focal disruptions of the endothelial monolayer (EM), through spatially resolved permeability assays and the proteomic characterization of tumor secretomes. Here, we present (i) the model's validation using a functional and mechanical assay; (ii) the comparison of two solid tumor cell lines with very distinct mechanisms to interact with the blood microvasculature —pancreatic ductal adenocarcinoma (PANC-1) and lung adenocarcinoma (A549)-; and (iii) the analysis of the exerted effects on the 3D EM through the physical and biochemical stimuli of solid tumors. This approach provides a unique opportunity to dissect the contribution of mechanical stresses to endothelial barrier dysfunction and to explore new mechanobiological strategies for vascular normalization. By isolating the effects of tumor-derived mechanical and biochemical factors in a physiologically relevant setting, this model bridges a critical gap in the study of vascular dysfunction within the TME.

2. Materials and methods

2.1. Cell culture

Human Umbilical Vein Endothelial Cells (HUVECs, RRID: CVCL_0F27) (C2519A, Lonza) were cultured in completed EGM-2 medium enriched with ascorbic acid, human Epidermal Growth Factor (hEGF), 2% Fetal Bovine Serum (FBS), Gentamicin Sulfate/Amphotericin (GA-1000), heparin, hydrocortisone, R3 Insulin-like Growth Factor 1 (R3 IGF-1) and Vascular Endothelial Growth Factor (VEGF) (EGM-2 medium, Lonza, Switzerland). HUVECs were cultured on 0.01mg/mL fibronectin-coated dishes (0.01mg/mL) in EBM2 complete medium (Lonza) supplemented with EGM-2 SingleQuots (Lonza) for a maximum of 8 passages. Pancreatic ductal adenocarcinoma cell line PANC-1 (RRID: CVCL_0480) and lung adenocarcinoma cell line A549 (RRID: CVCL_0023) (CRL-1469 and CCL-185, respectively, ATCC) were cultured in DMEM High Glucose (Invitrogen), supplemented with FBS 10% (Invitrogen), L-Glutamine 2mM (Lonza), and 100U/mL Penicillin, Streptomycin, and Amphotericin B (Lonza).

Tumor spheroids were generated from single-cell suspensions of PANC-1 or A549 cells under anchorage-independent conditions. This method does not allow precise control over the exact number of tumor cells per spheroid, as sphere growing process presents some variability. In order to reduce variability between experiments, cultures were always initiated with mechanically disaggregated cells from a previous suspension cultures and seeded at a density of 3 × 10^5 cells/mL in DMEM/F-12 GlutaMAX™ medium supplemented with 2% B27 (Gibco), 100 U/mL penicillin, streptomycin, and amphotericin B (Lonza), and 20 ng/mL FGF-basic (Pan-Biotech, Aidenbach, Germany). Cultures were maintained for 72 h, and visually proper spheroid formation was confirmed (Fig. S1). Next, spheroids were gently homogenized in suspension, and a standardized volume (1mL) was collected for each condition. This suspension was centrifuged at low speed (200rpm, 3min, 4°C) to obtain a pellet, which was resuspended in fresh DMEM-F12 and incorporated into the hydrogel following the procedures described below. This procedure ensured comparable spheroid densities between replicates, facilitating reproducibility across experiments.

To prevent cell adhesion, flasks were coated with 10% poly(2-hydroxyethyl methacrylate) (pHEMA, Sigma-Aldrich) in 96% ethanol, following established protocols [35]. pHEMA is a widely used biocompatible coating that provides a non-adherent surface, thereby facilitating spheroid formation [35–37]. As cells cannot attach into the pHEMA coated surface, they grow into spheres. Prior to cell seeding, flasks were rinsed once with PBS to remove excess coating.

All cell lines were grown in a humidified incubator at 37°C with 5% CO_2 and regularly tested for mycoplasma. Cells were confirmed to be contamination free via PCR detection which was performed using a real time PCR thermocycler (Bio Rad: Applied Biosystems CFX96 Real Time System) and visualized with gel imaging system (Bio Rad: ChemiDoc XRS+).

2.2. Microfluidic device microfabrication

Microfluidic devices were fabricated by casting polydimethylsiloxane (PDMS) onto silicon master molds. PDMS and curing agent were mixed at a proportion of 10:1, and, after vacuum degassing, the mix underwent polymerization at 80°C to create an elastomer-negative mold. The resulting mold was trimmed, and holes were punched to serve as ports for the hydrogel and media (Fig. 1B and 1C) [34,38]. Individual PDMS devices were autoclaved for sterilization, dried at 80°C overnight, and then bonded to coverslips using oxygen plasma (Harrick plasma, UK). Prior to bonding, PDMS devices and glass

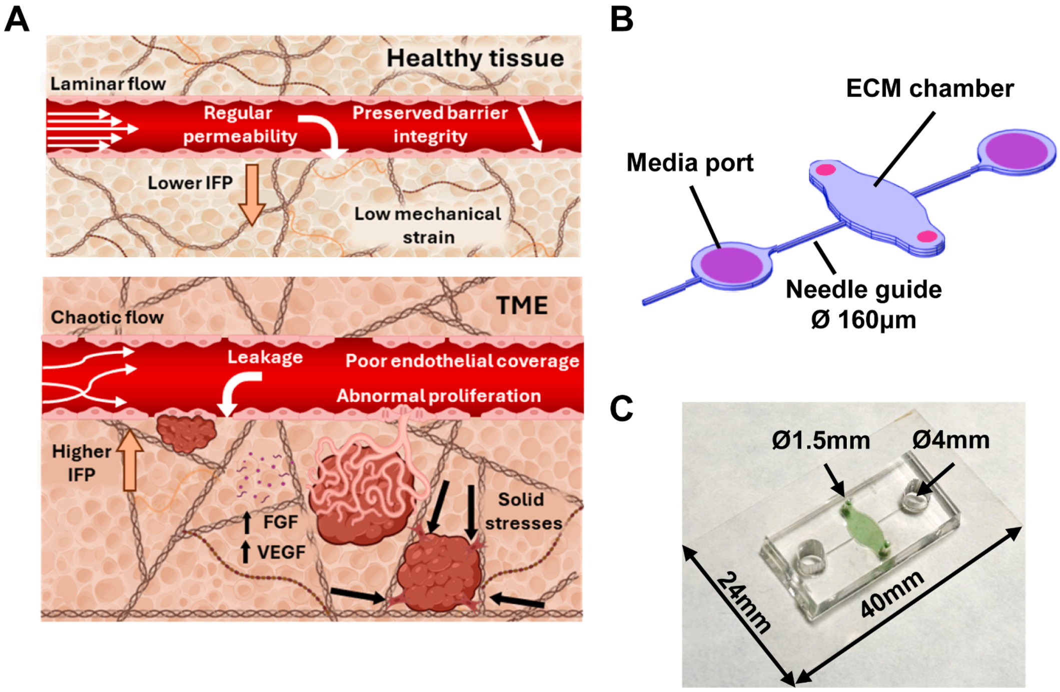

Fig. 1. Microfabricated vessel-on-a-chip platform. A) Schematic about the main mechanical and biochemical cues that compromise microvasculature barrier function with healthy tissue (top) and tumors (bottom). TME tumor microenvironment, IFP interstitial fluid pressure, FGF fibroblast growth factor, VEGF vascular endothelial growth factor. B) Schematic design of the microfluidic device, indicating the main ports and features. ECM extracellular matrix. C) Picture of device bonded to a 24mm × 40mm glass coverslip. The ECM chamber is stained in green.

coverslips were treated in an air plasma cleaner (30W, 120s, room air flow ∼1.33mbar). Immediately after exposure, both surfaces were brought into contact. Surface functionalization of the PDMS and glass was performed to enhance ECM binding. The functionalization was based on a polydopamine coating at 2mg/mL, as previously described [39]. Then, the microfluidic devices were rinsed and dried at 60°C in the oven for 24h to restore surface hydrophobicity.

2.3. *Lumen formation and HUVEC seeding*

After fabrication, stainless steel needles (0.16mm diameter × 40mm length, Seirin, Japan) were introduced via the needle guides within the microfluidic device before injecting the collagen hydrogel. These needles were previously coated with a 5% bovine gelatin solution for 30min at 37°C in order to facilitate detachment from the collagen matrix. Subsequently, reconstituted type-I rat tail collagen (Corning, USA) was prepared at a concentration of 2.5mg/mL from a stock solution of 4.33–3.43mg/mL and buffered to a pH of 7.4 with 1M of NaOH in sterile H_2O, as stated in Pérez-Rodríguez et al. [34]. The hydrogel solution was prepared in a mix of completed EGM-2 medium with 10X DPBS with phenol red and introduced into the devices through the central chamber ports, with the needle inserted. Devices were then moved to a humidified incubator at 37°C (5% CO_2) for at least 30min for hydrogel polymerization, and then medium ports were filled with completed EGM-2 to avoid dehydration. After 2h, needles were gently removed, creating a cylindrical lumen in the collagen matrix. Then, devices were sealed using Reprorubber (Flexbar, USA) and reservoirs were filled again with cell medium. The devices were placed on a laboratory rocker within the cell incubator to wash the lumen for 24h.

After lumen formation, a 0.01mg/mL human fibronectin solution was added through the medium ports to coat the formed lumen walls for 45min, increasing endothelial cell adhesion in the subsequent steps. Next, HUVECs were seeded into the lumen through the reservoir at a cell density of 4×10^6 cells/mL and allowed to form a cylindrical EM. Cell adhesion was observed with an inverted microscope, and devices were kept within the incubator for a maximum of 72h. As previously described, when the lumen reached an adequate cell density adhered to its walls, the cellular suspension was replaced with fresh medium, and devices were placed on a rocking platform within the incubator to generate gravity-driven oscillatory flow, as described in the literature [40,41].

2.4. *Quantification of tumor-induced lumen remodeling*

To assess the hydrogel structural changes due to the tumor spheroid-derived mechanical forces, microfluidic devices were manufactured as described above. Tumor spheroids were added to the hydrogel matrix (Fig. 2C), and EGM-2 medium was replaced with DMEM/F-12 containing spheroids obtained from a standardized suspension, ensuring reproducible loading conditions.

Without vessels, three experimental conditions were assessed: PANC-1 spheroids, PANC-1 spheroids treated with 50µM Blebbistatin, and A549 spheroids. Blebbistatin treatment was initiated 2h post-hydrogel polymerization by adding the inhibitor to the culture medium and perfusing it through the hydrogel lumen. The inhibitor-containing medium was renewed at 36h with the same concentration (50µM) (Fig. S1). Devices were maintained in a cell incubator for 72h, after which lumen diameters were measured. This approach enabled assessing the contribution of actomyosin-driven contractility to the observed remodeling.

To account for the contribution of endothelial forces, additional devices were prepared by seeding HUVECs into the preformed lumen 24h after hydrogel polymerization. These conditions included empty hydrogels (HUVECs only) and spheroid-containing hydrogels (either PANC-1 or A549 spheroids).

For quantification, images were acquired at the mid-transverse plane of each lumen at 72h, where the channel ran vertically through the field of view. A single optical section corresponding to the central plane was taken per device at 72h post-spheroid seeding using an inverted microscope (Eclipse Ti-E, Nikon). Multiple diameter measurements were taken in 2D cross-sectional images from one side of the EM to the other,

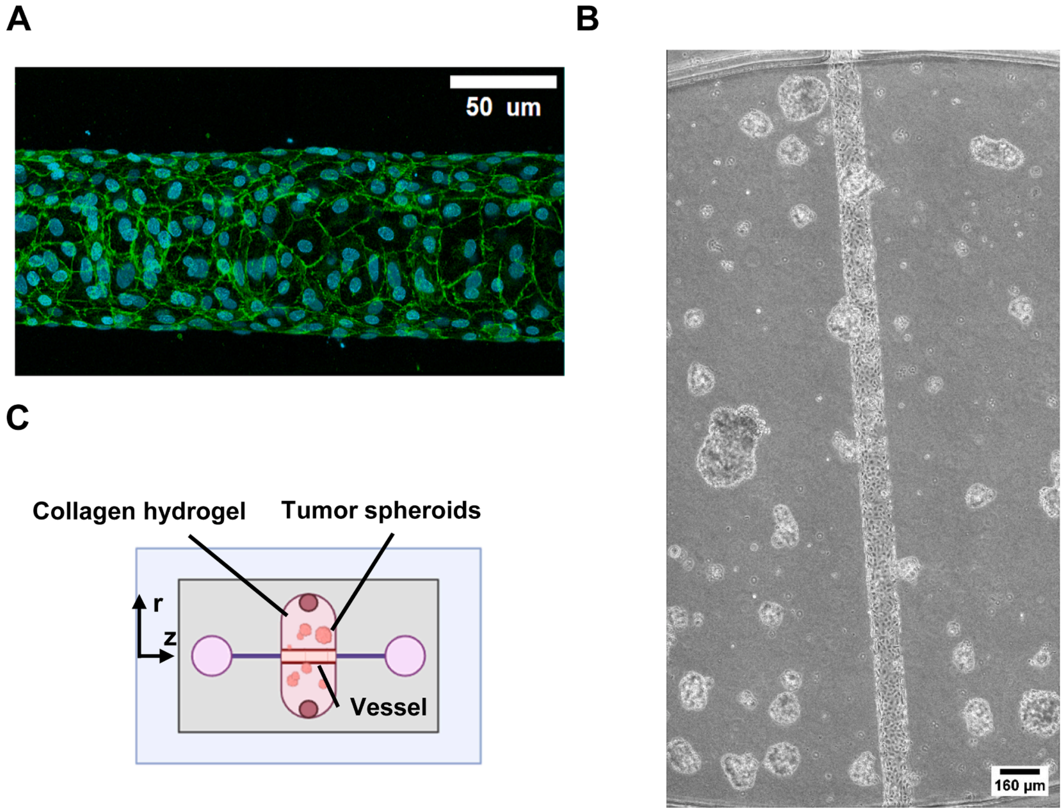

Fig. 2. 3D endothelial vessel co-cultured with tumor spheroids in the microfluidic device. A) 3D HUVEC vessel embedded in a collagen hydrogel. VE-Cadherin staining (green) highlights endothelial junctions and DAPI (blue) labels nuclei. PANC-1 spheroids (DAPI-only) are visible in the peripheral region. Scale bar: 50µm. B) Bright-field picture showing hydrogel chamber inside the microfluidic device, with the endothelial vessel and tumor spheroids distributed within the matrix. Scale bar: 160µm. C) Schematic representation (not to scale) of the device, indicating the position of the engineered vessel and tumor spheroids within the central chamber.

assuming cylindrical geometry, using Fiji software, and results were averaged across at least three independent devices per condition [42]. Although local asymmetries could occasionally be detected, remodeling typically spanned a continuous region of the lumen, maintaining an overall quasi-cylindrical geometry suitable for diameter-based quantification. Measurements were performed across replicate devices analyzed at each endpoint rather than longitudinal tracking of the same channel over time. Thus, the reported lumen size differences represent condition-dependent effects across parallel devices, not dynamic remodeling within a single device.

To minimize operator bias, the full image dataset was independently re-analyzed by a second researcher. A Bland–Altman comparison confirmed agreement between measurements, supporting the reproducibility of the remodeling quantification.

2.5. *Preparation of conditioned media*

PANC-1 and A549 cells were cultured at a density of 3×10^5 cells/mL in T25 flasks in anchorage-independent conditions, as described in Section 2.1. Complete DMEM-F12 medium was added to the culture and harvested after 72h of incubation. Each batch was concentrated using centrifugal filter units (Amicon Ultra-4, 10kDa cutoff, Merck) at 4000rpm, 4°C, for ~1.5–2h, until the volume was reduced to ~1/8 of its initial value. The concentration step was achieved exclusively by centrifugation through the filter membranes, without evaporation. Total protein quantification was performed by Bradford assay according to seller's instructions (Quick Start Bradford 1X Dye Reagent, BioRad). Concentrated conditioned medium preparations were stored at −80°C until use.

For experimental assays, CM was diluted in EGM-2 at final concentrations of 0.1% and 10%, depending on the experiment. As controls, vessels or HUVEC monolayers were cultured in EGM-2 alone (baseline control medium), or in EGM-2 supplemented with DMEM-F12 (supplemented control medium). Unless otherwise stated, CM-supplemented media and controls were applied for 48h before analysis.

2.6. *Immunostainings*

EM were washed with PBS and then fixed with 4% paraformaldehyde (PFA) at room temperature (RT) for 30min on an orbital shaker. Then, they were rinsed with PBS and permeabilized with 0.1% TritonX (Sigma-Aldrich) for 20min and blocked with a 5% BSA solution at RT for 2h. Afterwards, primary and secondary antibodies were diluted in a 0.1% BSA solution and added over-night or for 2h, respectively. Additionally, most samples were stained with 4′,6-diamino-2-fenilindol (DAPI) (1:1000, ThermoFisher) at RT for 20min. The devices were washed with PBS to remove fluorescent background before confocal microscopy. Images were acquired with a confocal microscope (Leica, STELLARIS LightSheet (DLS)).

2.7. *Imaging and permeability assays*

Endothelial permeability was quantified by measuring the diffusive transport of 70-kDa FITC-Dextran across the vessel wall using confocal time-lapse microscopy. EGM-2 medium was supplemented with 70-kDa FITC-Dextran (200µg/mL) and introduced into the vessels, maintaining equal volumes at both media ports to avoid flow-driven perturbations. Images were acquired at 10× magnification every 5 s for 10 min at the mid-transverse plane of the vessel. Fluorescence intensity was assumed to be proportional to solute concentration, allowing calculation of the diffusive permeability coefficient (P_d, see supplementary materials (S2)), as described by Polacheck et al. [38].

In order to spatially resolve variations in solute diffusion and quantify localized endothelial permeability, the R_{50} parameter was computed. R_{50} is defined as the radial distance from the vessel lumen at which the normalized fluorescence intensity in the ECM reaches 50% of the intravascular signal. To calculate this parameter, ±40μm regions around the defined upper and lower vessel boundaries were selected (Fig. S2), restricting the analysis to the perivascular zone and minimizing contributions from dextran diffusion deeper into the hydrogel. Each vessel provided two complementary walls, and thus, both were analyzed simultaneously, creating a “top” and “bottom” analysis. For each vertical column of pixels within these regions, the radial position where the normalized intensity crossed 0.5 was determined for every frame, providing a spatiotemporal measure of fluorophore penetration from the vessel into the ECM.

Mean pixel intensity in the ECM (I_{ECM}) was calculated for each frame and along the longitudinal vessel axis, and the corresponding diffusive permeability coefficients (P_d) were derived from the temporal changes in I_{ECM}, normalized by vessel radius and intraluminal intensity (I_{vessel}), as described in Eq. 4 (S2). This approach allows quantitative detection of variations in endothelial barrier function across different experimental conditions and provides an indirect but spatially informative readout of local permeability.

R_{50} values were visualized as two-dimensional heatmaps, with the horizontal axis representing the vessel longitudinal coordinate (z), the vertical axis representing time, and the color scale indicating the R_{50} value in micrometers (Fig. S2). These heatmaps provide a spatiotemporal representation of FITC-Dextran penetration along the vessel, capturing both localized heterogeneity and dynamic changes in permeability over the course of the assay. Representative frames with intensity profiles and R_{50} traces were also extracted to highlight specific spatial and temporal patterns.

All image acquisition and analysis steps were performed using a custom MATLAB script. Images were imported as 8-bit .tif files and normalized to a 0–1 intensity range. Vessel boundaries were manually delineated on a reference frame, and the perivascular regions were automatically extracted for further analysis. The script computed R_{50} for each column of pixels over time, generated heatmaps, and exported R_{50} matrices and P_d values for downstream statistical analysis. This automated pipeline enabled a robust, reproducible quantification of endothelial barrier function, integrating both local (radial) and longitudinal (along the vessel) information (see Supplementary Fig. 2).

Full image acquisition parameters, equation derivations, and MATLAB code details are provided in the supplementary materials (S2).

2.8. Proliferation and metabolic assays

HUVECs were seeded at a density of 1 × 10^4 cells/mL in 0.01mg/mL fibronectin-coated 96-well plates and allowed to adhere for 24h before treatment. Cells were then cultured for 5 days in EGM-2 supplemented with either control media or tumor-derived conditioned media (CM) from PANC-1 or A549 spheroids, as described in Section 2.5.

Metabolic activity was assessed using the resazurin-based alamarBlue® assay (Thermo Fisher). At 96h, 10% (v/v) alamarBlue reagent was added to each well, and plates were incubated for 2h at 37°C. Fluorescence was measured at 560/590nm (excitation/emission) using a microplate reader (SynergyLX, Biotek). Results were normalized to the baseline medium control (EGM-2 only).

Proliferation was quantified by cell counting. Fluorescence images were acquired at 96h using an inverted microscope (Eclipse Ti-E, Nikon). Nuclei and cell boundaries were automatically segmented using the Cellpose plugin implemented in ImageJ [37,38], and total cell numbers per well were extracted. For cell density analysis, images covering fields of view of 290×290μm were used, with multiple representative regions per well. At least three independent biological replicates, each with technical replicates, were analyzed to account for post-seeding distribution variance.

2.9. Morphological and junctional analysis of HUVEC monolayers

To assess the impact of tumor-derived secretomes on endothelial morphology and junctional organization, HUVECs were seeded at a density of 4 × 10^4 cells/mL in 0.01mg/mL fibronectin-coated 96-well plates to allow the formation of a confluent monolayer at time 0. After 24h, cells were exposed to the different media conditions described in Section 2.5 for 48h. Afterwards, cells were fixed with 4% paraformaldehyde for 15min at room temperature, permeabilized with 0.1% Triton X-100, and stained with anti-VE-Cadherin antibody (1:100, Santa Cruz).

For morphological descriptors, fluorescence images were acquired using a confocal microscope (Leica, STELLARIS LightSheet (DLS)), and quantitative shape descriptors (cell area and circularity) were extracted using Cellpose detector plugins in ImageJ [42,43]. For junctional analysis, images were acquired under identical exposure conditions, and junctional patterns were qualitatively assessed. Quantification of cell area and circularity was performed on at least three independent biological replicates.

2.10. Proteomic analysis

Protein digestion was performed using a standardized protocol (iST kit, PreOmics), and peptide concentration was measured by a fluorometric assay (Qubit 3.0 fluorimeter, ThermoFisher). Importantly, the proteomic analysis was conducted on conditioned media (CM) collected from PANC-1 and A549 cells cultured as described in Section 2.5, harvested 72h post-seeding and concentrated using centrifugal filter units, prior to any dilution in EGM-2 or application to endothelial cells, ensuring that the analysis reflected only the tumor cell secretome.

Samples were analyzed by LC-MS/MS using a TIMS-TOF system coupled to an EvoSep ONE chromatograph, acquiring profiles of loaded digested proteins using the 60 samples per day protocol. Peptide identification was carried out with PaSER software (Bruker Scientific LLC, 2023b), using a human protein database and standard decoy-based false discovery filtering (FDR $<$ 1%). Additional validation steps, including collisional cross-section scoring, ensured high-confidence identifications. Full acquisition parameters and data processing details are provided in the supplementary materials (S3).

2.11. Statistical analysis

All experiments were performed with at least three replicates performed in three independent biological assays unless otherwise stated. Generally, data are presented as the mean of independent experiments, each corresponding to one biological replicate. To provide additional transparency on data variability, pooled single-point values from all replicates are displayed in violin plots, which illustrate the full distribution underlying the summary statistics. Statistical significance was assessed using one-way or two-way ANOVA followed by Tukey’s post-hoc test, or unpaired two-tailed Student’s *t*-test for pairwise comparisons, as appropriate (GraphPad Prism v.8, GraphPad Software, San Diego, CA, USA). Differences were considered statistically significant at $p \leq 0.05$. All p-values are reported in APA style.

3. Results

3.1. Lumen remodeling assay within the TME-microvasculature model

In this study, a microfluidic set up was developed to simulate TME stimuli into microfabricated BEC vessels (Fig. 2A and B). To do so, PANC-1 and A549 spheroids were embedded in 2.5mg/mL collagen matrices to compare their distinct mechanical behaviors. Their mechanical effects on the microfabricated lumen were initially evaluated. Deformations exerted by the tumor spheroids were assessed by measuring changes in the width of the microfabricated lumen after 72h, prior to HUVEC seeding.

After 3 days, lumens in microfluidic devices containing PANC-1 spheroids were significantly larger (mean diameter 175±7µm) than lumens in devices with A549 spheroids (159±6µm) (n = 3, Fig. 3A). Treatment of PANC-1 spheroids with Blebbistatin (50µM) reduced lumen diameters to 159±6µm, comparable to the initial theoretical diameter of 160µm (Fig. 3A), confirming that PANC-1-mediated remodeling depended on cytoskeletal contractility.

Next, we wondered whether this deformation found in the lumen is compensated in the human body by other mechanical stimuli such as the physiological cell contraction in the EM of vessels. Hence, perfusable blood vessels with HUVEC EM were microfabricated within 3D collagen lumens in our microfluidic device. Endothelial cells were seeded 24h after hydrogel formation and measurements were taken after 48h, at which point the endothelial monolayer exhibited a consistent morphology. Vessels in hydrogels without spheroids showed significant narrowing (101 ± 23µm) due to HUVEC contractility (Fig. 3B). These results indicate that the endothelial cells exert forces within the hydrogel's surface, reducing significantly the microfabricated structure's width in comparison to its undeformed configuration (Fig. 3B).

After that, we co-cultured spheroids from both tumor cell lines next to the HUVEC monolayer, which revealed distinct mechanical interactions. BEC vessels within PANC-1 spheroids' hydrogels exhibited the largest variation, with a mean width of 190±34µm in diameter, reflecting heterogeneous lumens due to the complex interaction between the deformations exerted by the HUVECs and the tumor cells. In contrast, vessels co-cultured with A549 spheroids presented very homogeneous lumens with a mean diameter of 161±8µm. These results suggest that while endothelial cells reduce vessel diameter, A549 cell spheroids counteract this reduction, stabilizing the structure and maintaining lumen dimensions similar to those found in the undeformed configuration prior to any cell culture (Fig. 3B).

3.2. Impact of tumor spheroids on EM barrier's permeability in collagen matrices

Once confirmed that both tumor cell populations have an effect on the TME, since they exert counteracting forces that modify the vessel configuration, we wondered how both populations affect the structural integrity of the vessels. Thus, we analyzed the evolution of vessel permeability in the different conditions.

The barrier function of the EM was quantitatively characterized via the permeability coefficient (P_d) using 70kDa FITC-Dextran. A concentration of 200µg/mL was introduced in endothelial vessels within 2.5mg/mL collagen matrices (Fig. 4A). The fluorescent probe gradient was limited by the endothelial membrane, and measurements of fluorescence microscopy were taken every 5s for 10min in triplicates for each condition (n = 3). The fluorescence images revealed the trend of Dextran diffusion across the vessel at each time point (Fig. 4B). By quantifying changes in fluorescence intensity, the local diffusion of the fluorescence probe was quantitatively determined.

These assays showed significant differences in the diffusion of FITC-Dextran molecules through the membrane, modulated by the presence or absence of tumor spheroids (Fig. 4B). Without tumor spheroids, control vessels showed a low permeability coefficient (P_d= 0.03 ±0.02µm/s), indicating a more compact and efficient barrier function. These values correlate with the ones described previously in the literature [38,44]

In contrast, introducing tumor spheroids of PANC-1 and A549 cell lines resulted in a significant increase in vessel permeability. The quantitative analysis showed a significant increase in the permeability coefficient for A549 spheroids, with a value of 0.36±0.02µm/s, which resulted in a significant increase against the control condition ($p <$ 0.001, ANOVA). These results indicate that A549 spheroids induced a significant destabilization of the endothelial barrier integrity, potentially mediated by the secreted factors of the tumor spheroids. The permeability coefficient in presence of PANC-1 spheroids showed a drastic increase, resulting in a mean value of 1.4±0.2µm/s (Fig. 4C). These findings suggest a stronger disruptive interaction between pancreatic adenocarcinoma spheroids and the vessel, supporting the role of tumor-derived mechanical forces as a major driver of endothelial barrier disruption.

In addition, there is a strong spatial correlation between the presence of tumor spheroids and the local increase in the permeability of the BEC membranes (Fig. 4B). This effect is quantitatively demonstrated through the analysis of the R_{50} parameter, which represents the axial position where the normalized FITC-Dextran intensity reaches 50% of its value inside the hydrogel. In the R_{50} heatmaps (Fig. 4D), the horizontal axis represents the vessel length, the vertical axis the assay duration, and the

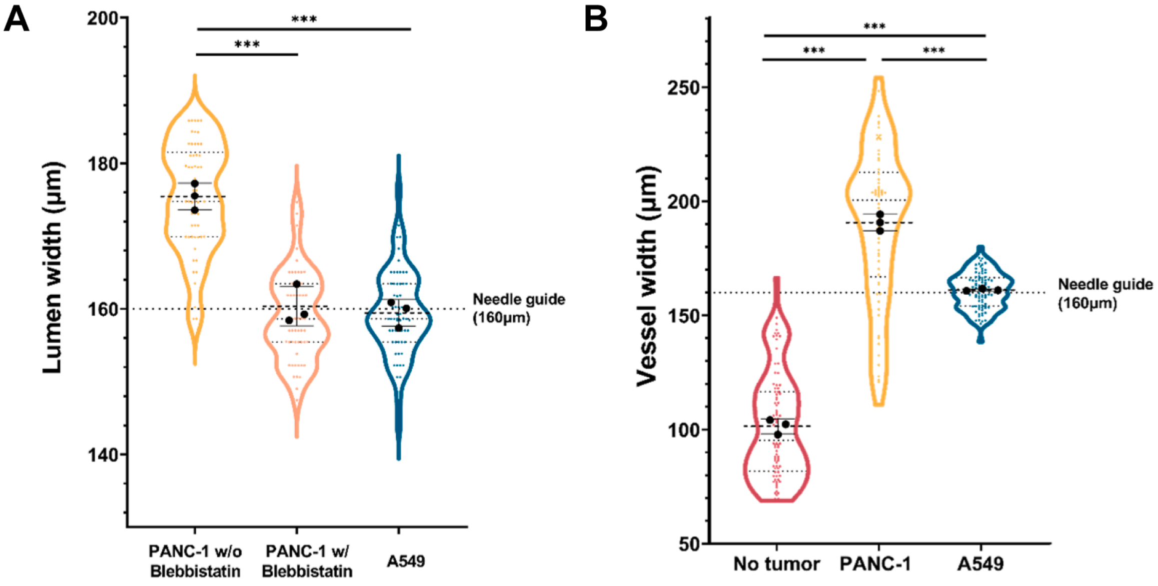

Fig. 3. Lumen remodeling assays within the TME-microvasculature model. A) Lumen widths on 2.5mg/mL collagen matrices with spheroids of PANC-1 w/o Blebbistatin treatment, PANC-1 w/ and A549. B) Vessel widths on 2.5mg/mL collagen with cultured HUVEC inside the lumen: empty matrices (no tumor) or seeded with PANC-1 and A549 spheroids. In both cases, widths are represented in violin plots with median, 25% and 75% quartiles. P-value reported in APA style (n = 3).

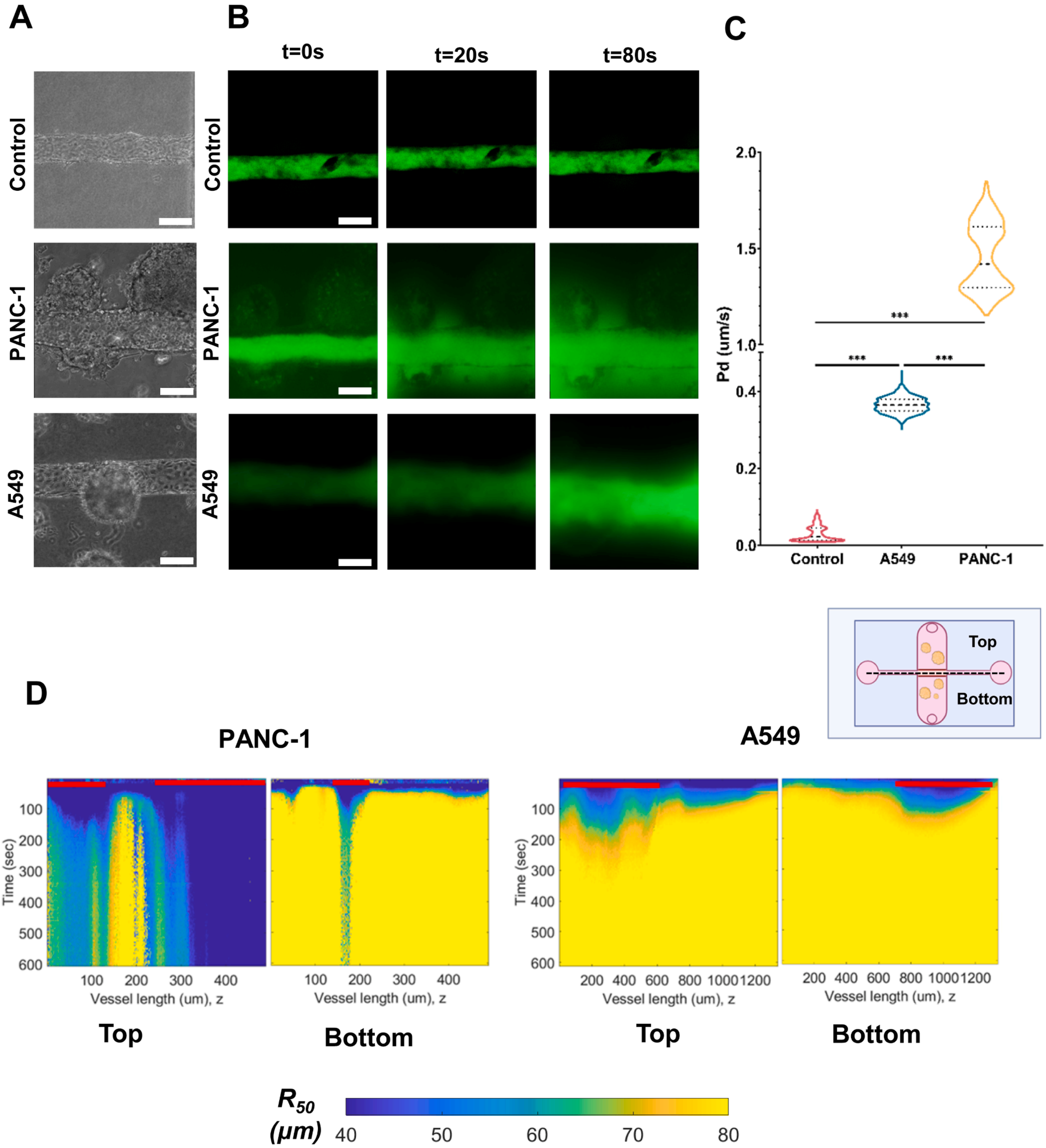

Fig. 4. EM permeability assays. A) Endothelial vessels in empty hydrogels, with PANC-1 and with A549 spheroids in 2.5mg/mL collagen matrices in brightfield. Scale bar is set at 160μm. B) Endothelial vessels in empty hydrogels, with PANC-1 and with A549 spheroids at different times (initial, 20s and 80s) of the FITC-Dextran assay. Pictures show the gradient of 70kDa FITC-Dextran permeating through the 3D endothelial membrane. Scale bar is set at 160μm. C) Permeability coefficient P_d values for all conditions tested, shown in violin plot. Statistical assessment was performed with a One-Way ANOVA and p-values are reported in APA style ($n = 3$). D) R_{50} Heatmaps of R_{50} values over time for vessels with PANC-1 (left) and A549 (right) spheroids. R_{50} quantifies the radial distance at which FITC–Dextran intensity decays to 50% of the intraluminal value, providing a spatially resolved measure of barrier leakage. Red horizontal bars indicate the longitudinal position of tumor spheroids relative to the vessel axis; they are shown for reference only and are not part of the R_{50} calculation.

color intensity indicates the R_{50} value (μm). Warmer colors correspond to higher R_{50} values, reflecting deeper solute penetration into the ECM and thus increased local permeability, while cooler colors represent lower R_{50} values and more restrictive barrier properties. Regions of the EM close to the spheroids presented a higher R_{50} in comparison to other areas, and evidence that at least half of the analyzed fluorescent probe had migrated beyond these points (Fig. 4D). This spatial distribution highlights the focal nature of the mechanical and chemical influence exerted by the tumor spheroids on the endothelial barrier. Notably, this phenomenon was particularly prominent in the PANC-1 spheroids, which is consistent with the global increase in the permeability coefficient under this condition.

3.3. Tumor-derived conditioned media as a disruptor of BEC's barrier permeability: effect of biochemical factors

The previous experiments demonstrated that tumor spheroids significantly alter endothelial permeability through both mechanical and biochemical interactions. However, it remained unclear to what extent soluble factors alone contribute to endothelial barrier dysfunction. To isolate the biochemical influence of the tumor secretome, we next investigated how conditioned media (CM) from PANC-1 and A549 cells affects vessel permeability in the absence of direct tumor-vessel interactions. By eliminating mechanical forces due to the tumors from the system, this approach allowed us to determine whether tumor-derived soluble factors alone are sufficient to compromise EM integrity.

In order to assess how the soluble factors secreted by the PANC-1 and A549 cell lines affect the permeability of the vessels in absence of the mechanical influence of the tumors, we performed permeability assays on microfabricated vessels in empty collagen matrices, which were cultured for 48h with CM-supplemented media. For this assay, concentrated CM from PANC-1 and A549 was diluted at 0.1% in EMG-2. As controls, vessels were exposed to the standard medium, EGM-2 and 0.1% DMEM-F12 supplemented media (Fig. 5A).

As described before, the control vessels showed a permeability coefficient of 0.03±0.02μm/s, values consistent with a compact and functional barrier integrity. However, the exposure to the CM from PANC-1 induced an increase in permeability up to 0.13±0.01μm/s. In a similar way, A549 derived CM increased the mean P_d of vessels to 0.11 ±0.02μm/s. Both values were significantly higher than the EGM-2 control measurements by a 3 or even a 4-fold increase, indicating that the soluble factors released from both tumor cell lines compromise directly the integrity of the endothelial barrier, even in absence of mechanical interactions among tumor and vessel (Fig. 5B). Nonetheless, both values were one order of magnitude lower than in the case where the spheroids were physically present in the hydrogel. Additionally, both conditions tested significantly higher than the DMEM-F12 controls. In contrast to the case in which tumor spheroids were present in the hydrogel, where the R_{50} heatmaps correlated more prominently with focal lesions in the endothelial barrier, the heatmaps obtained from this

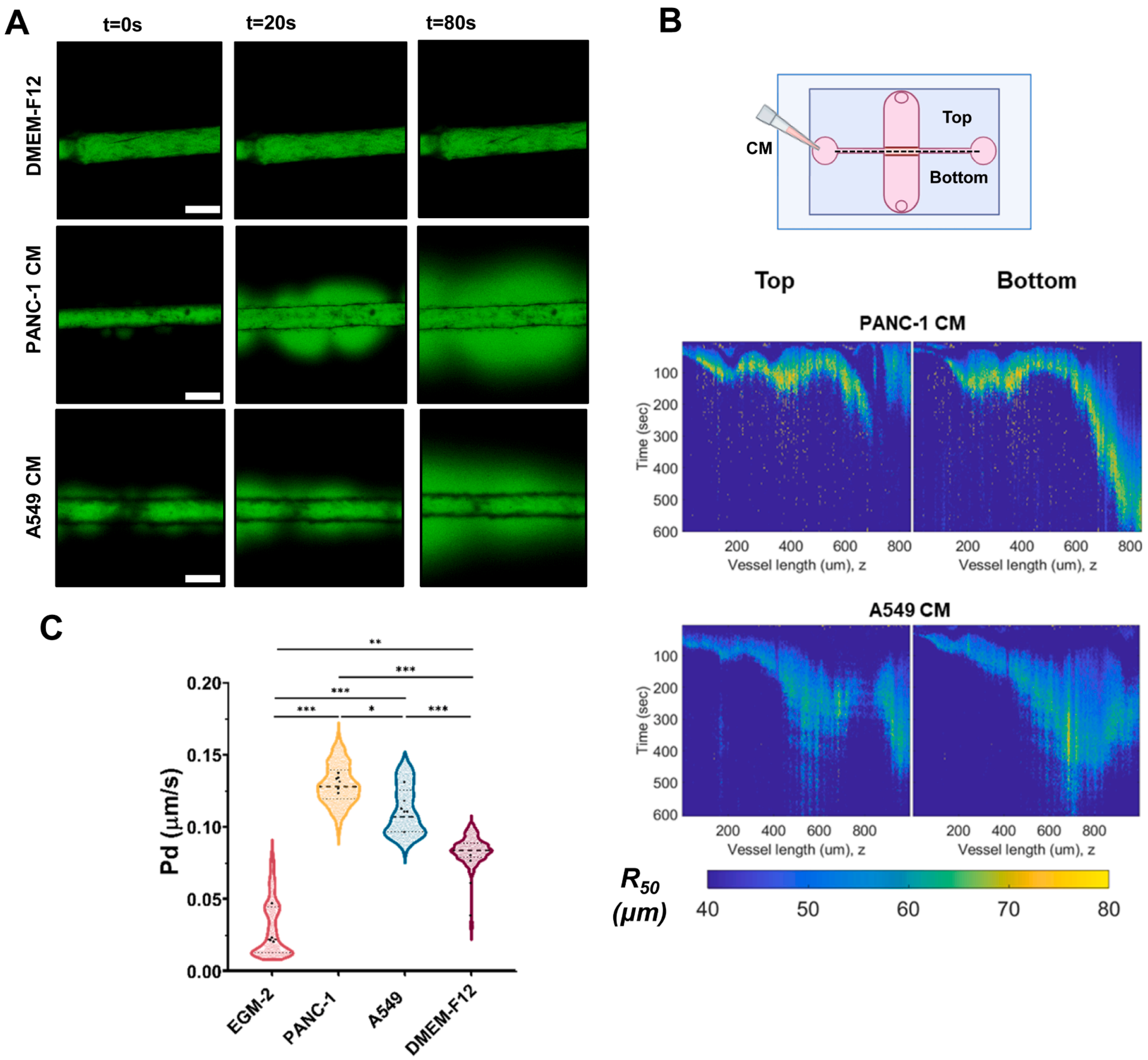

Fig. 5. EM permeability assays with conditioned medium (CM). A) FITC-Dextran assay. Up to down, endothelial vessels treated with EGM-2 supplemented with DMEM-F12, with EGM-2 supplemented with PANC-1 or with A549 CM at different times (initial, 20s and 80s). Pictures show the gradient of 70 kDa FITC-Dextran permeating through the 3D endothelial membrane. Scale bar is set to 160μm. B) R_{50} representations of BEC vessels treated, PANC-1 (top) and A549 CM (bottom). C) Permeability coefficient P_d values for all conditions tested, shown in violin plot. Statistical assessment was performed with a One-Way ANOVA and p-values are reported in APA style ($n = 3$).

analysis were more diffuse (Fig. 5C). The results show a more homogeneous distribution of permeability values, giving only hypothetical hints on the presence of micro-lesions or more lose cell-to-cell junctions areas.

3.4. Tumor-derived conditioned media mimics TME effects on EM proliferation and mechanics

Once proven that tumor-derived conditioned media (CM) from tumor cells significantly compromises endothelial barrier integrity, we next sought to determine whether these soluble factors also modulate other endothelial properties, such as proliferation and morphology. Given that tumor-secreted factors are known to influence endothelial cell behavior beyond permeability regulation, we assessed how CM affects HUVEC metabolic activity, growth dynamics, and structural characteristics in a 2D monolayer. By isolating the biochemical influence of tumor-secreted factors, this approach allowed us to further elucidate the role of soluble cues in shaping BEC function within the TME.

To determine this, HUVEC cells were cultured on 0.01mg/mL fibronectin coated 96-well plates for 5 days in order to evaluate their proliferative response to CM from PANC-1 and A549 tumor cell lines cultured in DMEM-F12 ($n = 3$). CM was concentrated using ultracentrifugation (8-fold concentration factor) and subsequently diluted into the conventional HUVEC medium (EGM-2). HUVEC were seeded at low density (10^4 cell/mL) and after 24h, CM or control conditions were applied to each well. For this approach, seven experimental conditions were tested: (1) EGM-2 alone (baseline medium control), (2) EGM-2 supplemented with 0.1% concentrated DMEM-F12, (3) EGM-2 supplemented with 10% concentrated DMEM-F12 (supplemented medium controls), and (4–7) EGM-2 supplemented with 0.1% or 10% CM from PANC-1 or A549 cells. The inclusion of DMEM-F12 supplemented conditions provided reference benchmarks for nutrient-driven effects, due to the presence of h-FGF and B27 known to support HUVEC proliferation, survival, and angiogenic activity [45,46]. This experimental set up allowed us to isolate the specific effects of tumor-derived CM.

The redox metabolic assay with alamarBlue® probe revealed that both tumor-derived CM and the supplemented medium control at 10% increased the metabolic activity of HUVECs, compared to the baseline medium control. Notably, A549 CM continued to enhance HUVEC metabolism even at 0.1%, highlighting its potency at lower concentrations (Fig. 6B). In contrast, at this concentration, neither the supplemented medium control nor PANC-1 CM showed significant differences versus the baseline medium control. When comparing the metabolic activity across concentrations, we observed that the supplemented medium control exhibited the largest decrease in viability when diluted to 0.1%, whereas PANC-1 and A549 CM showed lesser reductions. These findings suggest that the secretory profiles of PANC-1 and A549 mitigate the decrease in viability caused by DMEM-F12 dilution. In summary, while DMEM-F12's effects are strongly concentration-dependent, the tumor cell secretome maintains metabolic activity even at lower concentrations.

We analyzed cell proliferation by cell counting using Cellpose detector plugins in ImageJ [42,43]. The results showed a significant increase in HUVEC proliferation upon exposure to CM and supplemented medium control media (Fig. 6C). The highest proliferation was observed in the DMEM-F12 10% condition with a 4-fold increase of cell proliferation compared to the baseline medium control case, while PANC-1 and A549 CM at 10% induced moderate increases of two- and two-and-a-half fold. At 0.1%, no significant differences were found compared to the baseline medium control. These results suggest that while CM promotes proliferation, its effect is attenuated by dilution, in contrast to the metabolic activity measurements.

Expanding on the proliferation and metabolic activity results, the impact of tumor-derived CM from PANC-1 and A549 cell lines on HUVEC morphology and area was also evaluated (Fig. 6D and E). Notably, DMEM-F12, at both concentrations of 0.1% and 10%, significantly increased the area of HUVECs compared to the control, indicating the impact of the factors present in this medium. Interestingly, while CM from PANC-1 and A549 did not significantly differ from the control at a 10% concentration, it significantly increased the area at a 0.1% concentration, suggesting that at this dilution, the tumor-derived factors are too diluted and behave similarly to DMEM-F12 at 0.1%. In contrast, at 10%, the factors in PANC-1 and A549 CM induce a significant decrease in the HUVEC area. The analysis of cell morphology revealed that HUVECs exposed to A549 CM exhibited a slightly lower circularity –a shape descriptor that indicates how closely an object resembles a perfect circle, with higher values indicating more circular shapes, which is defined as the area of the cell multiplied by four times pi and divided by the square of its perimeter–, both at 10% and 0.1% concentrations (Fig. 6E). This suggests that factors secreted by A549 cells promote a more elongated cell shape, indicating potential cytoskeletal remodeling or changes in adhesion dynamics induced by the tumor secretome. Additionally, as shown in Fig. 6A, VE-Cadherin staining patterns appeared visually less continuous in both A549 CM conditions and in PANC-1 CM at 10%, suggesting potential alterations in cell–cell junction organization. This observation was further supported by a quantification of junctional discontinuities (Supplementary Fig. 4). By contrast, DMEM-F12 (10% and 0.1%) and PANC-1 CM at 0.1% displayed VE-Cadherin distributions that qualitatively resembled the control condition, indicating a comparatively preserved endothelial barrier morphology.

3.5. Proteomic analysis of tumor-derived conditioned media reveals distinct TME interactions

In order to investigate the molecular basis behind the observed effects of the tumor-derived CM on BECs, we performed a proteomic analysis of PANC-1 and A549 cells secretomes. Both cell lines were grown in anchorage-independent conditions and the discovered proteins were analyzed by a pathways' enrichment analysis in Reactome database (version 91, retrieved 14th of march 2025) (Table S1) [47]. This method allowed us to identify the key biological processes that may be responsible for the observed differences in vessels' permeability and in BEC's proliferation and phenotype, proposed here as changes in cell morphology, organization, and functional behavior.

The results revealed a clear distinction between the remodeling strategies employed by A549 and PANC-1 cells, as shown in Fig. 7A. The proteomic profile of A549 CM revealed a strong enrichment in pathways associated with ECM degradation, immune activation, and complement system regulation. In particular, the results showed the ECM organization (FDR $= 1.7 \cdot 10^{-8}$) as one of the most enriched pathways (Fig. 7B). Within this pathway, several proteolytic enzymes such as MMP7 and ADAM10 were identified, which could be related to a strong ECM degradation (FDR $= 6.11 \cdot 10^{-5}$) process and a complex display of several cell-to-matrix adhesion molecules, respectively, contributing to a softening of the ECM.

Indeed, L1 family immunoglobulin, integrins, laminins, vitronectin and fibronectin were identified, justifying the presence of ADAM10 as cleaver of several of these adhesion molecules, facilitating the cellular reorganization of tumor cells within the spheroid and their interaction with collagen matrices. Additionally, A549 cells showed a significant enrichment in the complement cascade (FDR $= 7.00 \cdot 10^{-5}$), and other pathways such as innate immunity (FDR $= 1.21 \cdot 10^{-5}$) and neutrophil degranulation (FDR $= 6.29 \cdot 10^{-3}$) were also significantly upregulated, which suggests that A549 secretome induces endothelial activation and inflammatory responses (Fig. 7B).

In contrast, the PANC-1 CM proteome was enriched in pathways related to cytoskeletal remodeling, adhesion, and mechanotransduction. The most significant pathways included L1CAM interactions (FDR $= 1.59 \cdot 10^{-6}$) and the activation of IQGAPs by RHO GTPases (FDR $= 4.96 \cdot 10^{-6}$), both of which regulate cell adhesion, migration, and physical interactions with the ECM (Fig. 7B). Unlike A549, which degrades and

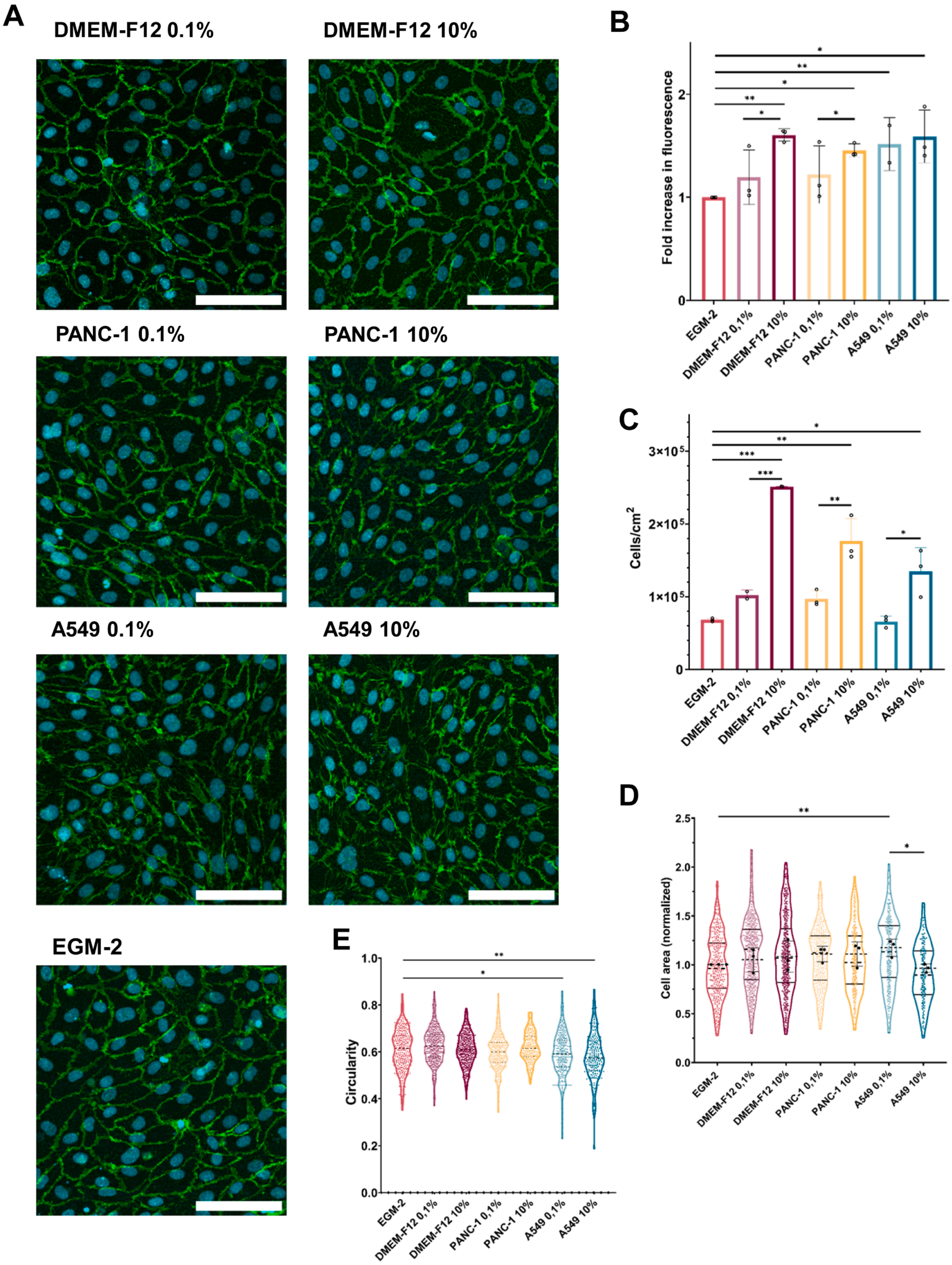

Fig. 6. Differential effects of tumor conditioned media on HUVEC proliferation, morphology and cell-to-cell adhesion. A) Fluorescence images of HUVEC monolayers treated with different CM. VE-Cadherin stained in green and nuclei in blue. Scale bar is set to 100μm. In EGM-2 control condition, an overlay of the segmentation with Cellpose plugin is shown. B) Metabolic assay results at day 4 expressed in fold increase of fluorescence to the control (EMG-2). C) EM density measured by nuclei counting in image analysis. D) Cells area measured with Cellpose plugin in ImageJ, normalized to EGM-2 control condition. E) Circularity parameter obtained from image analysis data. Normalized cell perimeter was segmented as an approximation, and thus, the data only correlates with elongation of the shape. Statistical assessment was performed with a One-Way ANOVA and p-values are reported in APA style (n = 3).

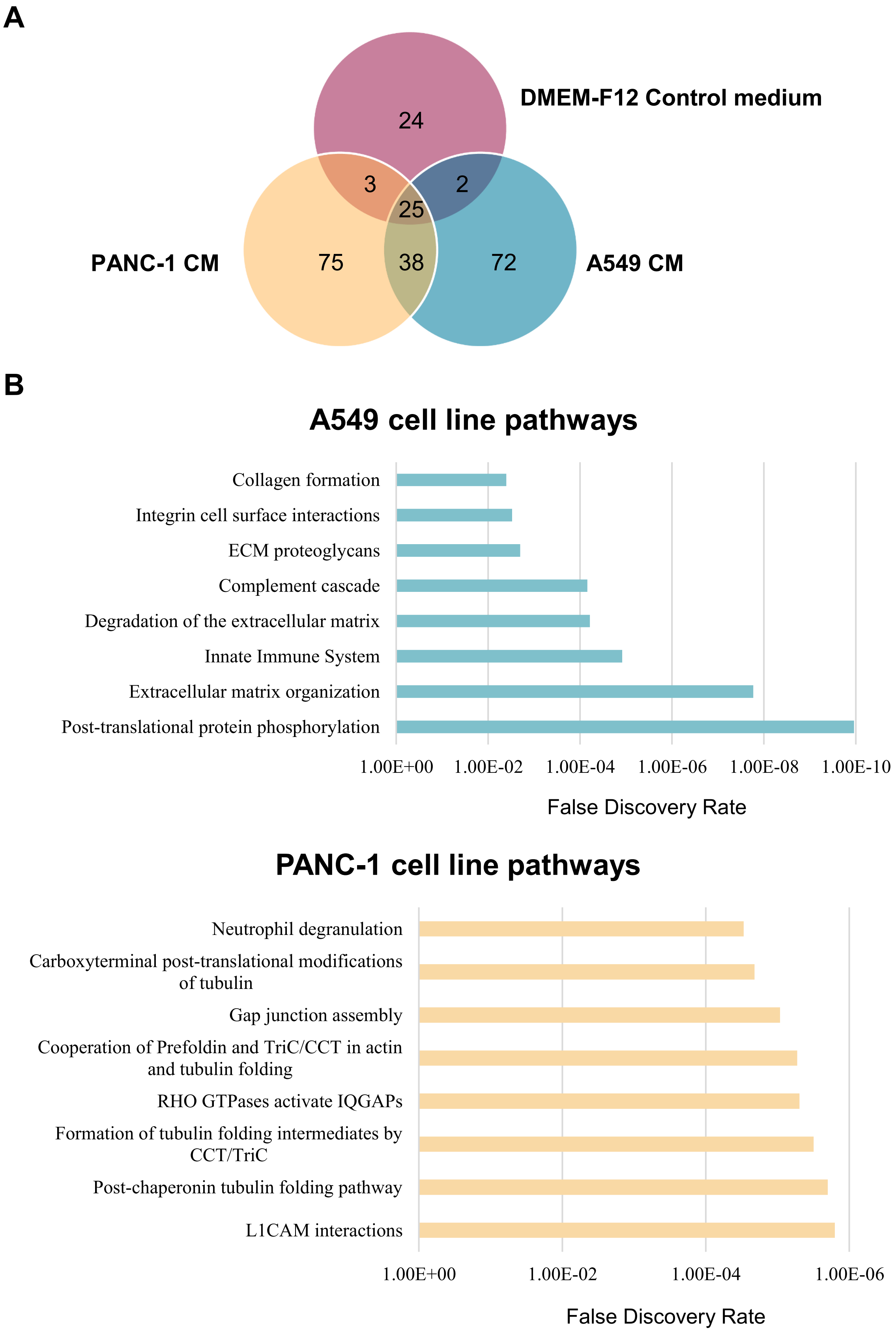

Fig. 7. Proteomic analysis data. A) Venn diagram of proteins found in common between the DMEM-F12 control media and the CM from PANC-1 and A549. B) Reactome (v.91) overrepresentation analysis. This method provides a statistical (hypergeometric distribution) test that determines whether certain pathways are over-represented (enriched) in the submitted data. Enriched pathways are represented by their predicted FDR.

modifies the ECM biochemically, PANC-1 CM appears to promote a mechanically engaged microenvironment, reinforcing adhesion and altering cytoskeletal dynamics.

The upregulation of L1CAM interactions further supports the idea that PANC-1 secretome enhances adhesion to the endothelium, potentially facilitating extravasation and metastasis. The enrichment in neutrophil degranulation (FDR $= 3.00 \cdot 10^{-5}$) suggests that, similar to A549, PANC-1 CM contributes to endothelial activation, though likely through different mediators. However, the absence of strong ECM degradation pathways in PANC-1 CM suggests that this cell line primarily interacts with its environment through force generation and adhesion rather than biochemical ECM remodeling.

In summary, the proteomic differences found in the secretomes of A549 and PANC-1 CM evidence the different strategies that tumors use to modulate their endothelial microenvironment, either through ECM degradation and immune activation or through mechanical stimuli derived from enhanced tumor cell adhesion and cytoskeletal remodeling.

4. Discussion

Tumor microvasculature is highly abnormal, exhibiting significant junction defects, poor pericyte coverage and altered morphology and functionality, which results in elevated membrane permeability, high IFP and tissue hypoxia [9–11] (Fig. 1A). Although conventional therapies inhibiting VEGF or Ang-2 aim to normalize these vessels, they often fail to restore barrier function and perfusion, partly due to overlooked mechanical forces within the TME [13,14,48].

Mechanobiological strategies targeting ECM stiffness, IFP, or shear stress may improve vascular function and drug delivery [9,21]. Despite the increasing recognition of tumor mechanobiology as a key factor of vascular functionality, the experimental models designed for precisely assess mechanical constraints within the tumor endothelium remain scarce. In the last decade, vessel-on-a-chip models have shown to be suitable tools for tissue engineering, as they allow to characterize the vascularization of several tissues [38,40]. However, in this work, we have focused on the interaction tumor-endothelium present in our modelled TME. Our results have demonstrated that mechanical forces and tumor-derived secretomes affect BEC vessels in a distinct yet synergistic way, providing a unique opportunity to explore innovative vascular normalization strategies through a mechanobiological perspective. While PANC-1 spheroids mainly act over their neighboring microvasculature through mechanical stimuli, our A549 spheroids present a more biochemical-driven interaction.

Our results show that EM in the absence of tumor spheroids exerted contractile forces, significantly reducing lumen diameter in soft collagen matrices. This behavior is consistent with previous reports showing that BECs dynamically modulate vessel size through a tension balance with the surrounding ECM, especially in compliant environments [49]. The observation made in our model aligns with previous findings demonstrating that the balance between BEC’s contractility and matrix mechanics is a key regulator for capillary structure [50,51]. Indeed, it has been shown that BECs dynamically adjust their vessel diameter depending on their ability to contract against the surrounding ECM, highlighting these cells as key mechanotransductive examples. However, our findings extend this concept by demonstrating that tumor spheroids can disrupt this mechanical equilibrium, leading to abnormal vessel morphology and increased permeability.

Our model revealed a stark contrast between the mechanical behaviors of PANC-1 and A549 spheroids. Both types of spheroids, despite forming sizable bodies in the collagen hydrogel, engage with their TME through fundamentally different mechanisms, shaping their microenvironment differently. While both formed sizable structures in the hydrogel, only PANC-1 spheroids significantly deformed the matrix, increasing vessel diameter by ~10%, whereas A549 spheroids induced negligible changes. This aligns with prior reports showing a strong myosin II-mediated contractility in pancreatic adenocarcinoma cell lines, which we further confirmed by reversing the deformation using Blebbistatin [52,53]. Consistently, Second-Hermonic Generation (SHG) imaging revealed that PANC-1 spheroids induced visible traction and reorganization of collagen fibers near the vessel, whereas A549 spheroids did not (see supplementary Fig. 3). This further supports that vascular disruption in the PANC-1 condition arises mainly from mechanical forces.

Dynamic time-lapse imaging was not performed in this study, however, capturing the temporal evolution of lumen remodeling following blebbistatin application would provide deeper insights into the dynamics of tumor-endothelial mechanical interactions. This represents an interesting direction for future investigations.

Moreover, the co-culture with endothelial cells appeared to amplify the mechanoresponse of PANC-1 cells, likely through matrix tension induced by the endothelial monolayer (see Section 3.1). This mechanical feedback loop underscores the high mechano-sensitivity of PANC-1 cells, which adapt their contractility in response to microenvironmental stiffness—likely via integrin-based mechanosensing [53].

Unlike PANC-1 spheroids, A549 spheroids exert minimal forces on the surrounding ECM, even in the co-culture with HUVECs. Rather than adapting to matrix stiffness, A549 cells actively remodel their surroundings through proteolytic activity and ECM protein secretion, as supported by their proteomic profile. This suggests that these cells reconfigure their microenvironment to adjust it to their own mechanical needs, rather than adapting themselves to the matrix properties. This remodeling likely softens the matrix and alters the biochemical milieu, reducing mechanical cues sensed by BECs and stabilizing lumen dimensions. This is consistent with their lower contractility and their reliance on biochemical interactions rather than physical interactions with the ECM [54]. Altogether, these effects may create a more permissive environment, fundamentally differing from the mechanical disruption observed in the pancreatic adenocarcinoma model.

While PANC-1 spheroids induced hydrogel and vessel deformation, these effects are unlikely to result from differential proliferation between tumor cell lines during the 72h assays. Cancer cells proliferate more slowly in 3D than in 2D cultures due to diffusion limitations and matrix interactions [55,56], and our recent work confirmed reduced proliferation and metabolic adaptations of A549 spheroids compared to 2D monolayers [57]. Notably, PANC-1 cells proliferate particularly slowly in collagen hydrogels, requiring several days to form spheroids from single cells [58]. Thus, the deformation observed here is better explained by tumor contractility, consistent with the reversal of vessel narrowing by Blebbistatin (Fig. 3A) and the ECM reorganization seen in SHG multiphoton images (Supplementary Fig. 3), rather than differences in proliferation or initial spheroid number. However, ECM remodeling, particularly through matrix metalloproteinases (MMPs) and other proteolytic enzymes, may also play a significant role in modulating lumen geometry. Indeed, our proteomic analysis on PANC-1 revealed enrichment of proteins related to ECM degradation and adhesion remodeling, suggesting that both mechanical and biochemical cues act in concert. Therefore, the observed deformations are likely the result of a combined effect of tumor contractility and ECM remodeling. Future work, including the use of broad-spectrum MMP inhibitors alongside contractility inhibitors, will be necessary to completely disentangle the relative contribution of these processes.

These differences seen in the lumen remodeling tests underscore how tumor type-specific microenvironments shape vascular interactions: pancreatic adenocarcinoma, growing in stiff, fibrotic matrices, disrupts vessels via mechanotransduction, while lung adenocarcinoma, in softer ECMs, drives remodeling through proteolytic and secretory pathways. Moreover, there was a sharp increase in vessel permeability observed with PANC-1 spheroids —nearly 50-fold over controls— that highlights the distinct mechanical mechanism through which this pancreatic adenocarcinoma model disrupts endothelial integrity. This effect is supported by R_{50} heatmaps, which revealed focal permeability hotspots near spheroids, consistent with direct matrix deformation and junctional destabilization. Such localized barrier disruption aligns with literature reporting that mechanical forces promote endothelial gap formation via Rho kinase signaling [59]. Conversely, A549 spheroids induced a moderate (~10-fold) yet significant increase in permeability, associated with a diffuse pattern of endothelial disruption.

Importantly, tumor spheroids were used instead of dispersed cells because they are known to alter vessel microenvironment [60,61]. This set up enabled the R_{50} analysis, which captures spatial alterations in endothelial permeability. Hence, spheroids provide a biologically relevant platform to study mechanotransductive and biochemical effects that would be missed in homogeneous cultures. However, we did not explicitly quantify spheroid positions along the vessel axis and therefore cannot rigorously correlate individual spheroids with local permeability changes. The observed distribution of R_{50} values suggests that spheroid proximity may influence endothelial barrier function, but a systematic spatial correlation incorporating spheroid segmentation will be necessary in future studies to quantify this relationship.

Proteomic analysis of A549 spheroids revealed strong enrichment in ECM-degrading enzymes and complement cascade components such as C1R, C1S, and notably C5, which promotes vascular leakage via PGE2-mediated signaling [59]. These findings reflect global biochemical effects on the endothelium and are consistent with the diffuse and homogeneous permeability patterns observed in R_{50} maps (Fig. 5C), suggesting that A549-induced barrier weakening is predominantly driven by biochemical signaling, rather than localized mechanical stress. The global endothelial activation and junctional destabilization seen in this condition can thus be attributed to a combined proteolytic and inflammatory environment established by the A549 secretome. Conversely, the proteomic profile of PANC-1 CM showed enrichment in adhesion- and cytoskeleton-related pathways, such as L1CAM interactions and IQGAP–RHO GTPase signaling, indicative of enhanced cell–matrix coupling and actomyosin-driven contractile activity, as evidenced by the Blebbistatin rescue. These molecular traits agree with the R_{50} permeability patterns, which point to mechanically driven disruptions near PANC-1 spheroids (Fig. 4D), and with the deformation observed in both the endothelial vessel and the surrounding collagen matrix. These molecular traits align permeability patterns suggestive of mechanical effects near PANC-1 spheroids (Fig. 4D), as well as with the observed deformation of the endothelial vessel and surrounding collagen matrix. These results suggest that these pancreatic tumor cells modulate endothelial permeability primarily through force transmission and mechanical disruption, complemented by moderate ECM remodeling.

These results underscore that the balance between mechanical contractility and ECM remodeling is tumor-type dependent and highlight the importance of integrating both perspectives when studying tumor–vessel interactions. The enrichment of proteolytic, adhesive, and inflammatory pathways in the respective models supports the proposed mechanobiological framework, in which tumor type–specific secreted factors determine whether barrier disruption arises from diffuse biochemical activation or localized mechanical stresses. Future studies incorporating replicated proteomic datasets and targeted inhibition of identified pathways (e.g., MMPs, complement components, or Rho-GTPase signaling) will be essential to validate and expand these mechanistic connections.

Taken together, our results highlight tumor-type–specific mechanisms in which PANC-1 spheroids primarily disrupt endothelial barrier function through mechanical forces complemented by moderate ECM remodeling, whereas A549 spheroids act predominantly through diffuse biochemical effects. While R_{50} mapping captures trends in spatial heterogeneity of permeability, the current study does not provide direct correlation between individual spheroid’s location and local endothelial defects. Future studies incorporating spheroid segmentation and endothelial proteomics will be essential to establish a causal link between tumor location, force transmission, and local barrier disruption.

To isolate the biochemical contribution of tumor secretomes, EMs were cultured with conditioned media (CM) derived from PANC-1 and A549 spheroids. Strickingly, both CMs significantly increased endothelial permeability –4-fold and 3.5-fold, respectively—despite the absence of direct tumor-vessel interaction, confirming the efficacy of soluble factors in compromising barrier integrity of EMs. However, these increases in vessel permeability seem negligible when compared to the ones obtained in the presence of tumor spheroids. Here, the permeability variable R_{50} heatmaps revealed diffuse and subtle increases in permeability along the vessel wall. Unlike the focal disruptions seen in Fig. 4D, CM exposure led to a more homogeneous pattern of barrier destabilization, supporting a globalized but less intense biochemical effect, as seen in Fig. 5C. Nevertheless, the observations of FITC-Dextran diffusion are still heterogeneous, even though this trait was substantially less pronounced than the observed in the presence of tumor spheroids. This heterogeneity can be easily attributed to the intrinsic dynamic reorganization of cell-to-cell junctions described at subcellular levels in EM [62]. In this context, the R_{50} analysis becomes a detailed local indicator of membrane functionality. Heatmaps generated from this parameter allow to identify specific regions with increased permeability, which could correspond with weaker areas of the membrane where the intercellular junctions have been destabilized by the secreted factors in the CM.

It is important to note that these findings were obtained in type I collagen hydrogels, selected for their relevance as the main component of tumor interstitial ECM. Although the global stiffness from these hydrogels preparations was relatively low ($G' \approx 62$Pa [63]), collagen networks exhibit strain stiffening under cellular traction, meaning that endothelial cells and spheroids experience a locally stiffer environment, closer to *in vivo* conditions [64,65]. Thus, while our conclusions are specific to collagen I, the mechanistic differences observed between PANC-1 and A549 spheroids are likely robust, though future work using matrices with varying stiffness and composition will be needed to confirm their generality.

Furthermore, tumor-derived secretomes, in addition to altering permeability, also influenced endothelial cell proliferation, metabolic activity and morphology. Both PANC-1 and A549 CM significantly enhanced metabolic activity in HUVECs, with A549 CM showing significant effects even at lower concentrations. This response likely reflects activation of glycolytic and other pro-survival metabolic pathways, such as FAO and amino acid metabolism, consistent with the metabolic reprograming seen in tumor BECs [66–69]. However, proliferation did not increase to the same extent: while DMEM-F12 at 10% induced the strongest growth in proliferation, PANC-1 and A549 CMs led to more moderate effects, suggesting that CM supports viability without fully mimicking the mitogenic potency of non-treated DMEM-F12 supplementation. Regarding EM formation, A549 CM significantly altered HUVECs morphology, slightly reducing endothelial cell circularity and promoting a more elongated shape at both concentrations tested. These changes indicate cytoskeletal remodeling, consistent with previous studies showing that tumor-conditioned media induces EC elongation and mesenchymal-like features [70]. Moreover, these observations align with Bourreau et al. [71], who reported that HUVECs exposed to conditioned media from A549 and other NSCLC lines undergo morphological changes, increased stress fiber formation, enhanced migration, and partial endothelial-to-mesenchymal transition, accompanied by a proteomic signature enriched in ECM remodeling and adhesion pathways. Also, CM from breast cancer cell lines has been shown to promote EC elongation and cytoskeletal reorganization, including the formation of stress fibers, which is associated with changes in cell adhesion and contractility. This alteration in morphology is associated with cytoskeletal remodeling, enhancing EC migration and tube formation, which are key processes in angiogenesis [72]. These angiogenic and permeability-related changes likely result from ECM proteoglycans and integrin-associated pathways identified in A549 CM proteomic profile, which may influence cytoskeletal dynamics and endothelial interactions within the matrix, priming the endothelium for further angiogenic responses. In contrast, VE-Cadherin staining appeared visually less continuous in both A549 CM conditions and in PANC-1 CM at 10%, suggesting potential alterations in cell–cell adhesion patterns, a trend also supported by the quantification shown in Supplementary Fig. 4. These findings suggest that tumor-secreted factors, particularly from A549 cells, may impair endothelial integrity by modulating adhesion molecule expression, consistent with previous research showing that lung adenocarcinoma secretomes destabilize endothelial junctions in BECs [71,72]. Future studies could further explore how the composition of 3D versus 2D tumor secretomes differentially impacts endothelial function. While our work directly demonstrates that 3D tumor secretomes modulate endothelial barrier integrity and morphology in a vessel-on-a-chip platform, comparative computational analyses of 2D and 3D secretomes would provide additional mechanistic insights. Such analyses could help identify specific secreted factors responsible for endothelial remodeling and guide the development of more physiologically relevant models for studying tumor–vascular interactions.

Taken together, our findings reveal two fundamentally distinct yet complementary mechanisms by which PANC-1 and A549 spheroids disrupt the endothelial barrier and remodel the tumor microenvironment. PANC-1 cells primarily exert mechanical forces, leading to vessel destabilization through cytoskeletal remodeling and adhesion molecule regulation, whereas A549 spheroids promote local permeability through the secretion of soluble inflammatory and proteolytic factors, including components of the complement cascade and ECM-degrading enzymes. These mechanistic differences have important therapeutic implications, suggesting that vascular normalization strategies should be specifically tailored for each tumor type. For pancreatic adenocarcinomas, targeting mechanotransduction pathways, such as RHO GTPases and L1CAM in the PANC-1 model, may help to counteract mechanically induced vessel disruption, while for lung adenocarcinomas, approaches aimed at inhibiting ECM degradation and complement activation could better preserve endothelial integrity. Ultimately, combining mechanobiological and biochemical modulation may offer more effective strategies for restoring vascular function depending on the specific characteristics of each tumor. Overall, our study underscores the necessity of integrating mechanical and biochemical perspectives in vascular normalization research and provides a framework for developing more effective, tumor-specific therapeutic strategies.

Data availability

Data is shared by the corresponding author upon reasonable request.

CRediT authorship contribution statement

Alejandro Martín-Contreras: Writing – original draft, Software, Methodology, Investigation, Formal analysis, Data curation. **María Sarasquete-Martínez:** Software. **José Manuel García-Aznar:** Writing – review & editing, Supervision, Resources, Funding acquisition, Conceptualization. **Alejandra González-Loyola:** Writing – review & editing, Supervision, Conceptualization. **María José Gómez-Benito:** Writing – review & editing, Supervision, Software, Funding acquisition, Conceptualization.

Declaration of competing interest

The authors declare that they have no known competing financial interests or personal relationships that could have appeared to influence the work reported in this paper.

Acknowledgements

European Union through European Research Council ERC-2023-POC, 101138214 – VASTO and ICoMICS Adv. Grant agreement ID: 101018587 (A.M-C., J.M.G-A., M.J.G-B., A.G-L.); Spanish Agency of research MCIN/AEI/10.13039/501100011033 grant agreement No PID2024-155426OB-I00 (A.M-C., M.J.G-B.) and ERDF European Union “A way of making Europe” grant agreement No PID2024-155426OB-I00 (A.M-C., M.J.G-B.). Instituto de Salud Carlos III (ISCIII) (IHMC22/00004) financed by the European Union – NextGeneration EU (A.G-L.); the Government of Aragon (Spain) Grant No 2022–26 (A.M-C.) and 2023–2027 (M.S-M.). Proteomic analyses were performed in the Proteomics Core Research Facility of Servicios Científico Técnicos del CIBA (IACS-University of Zaragoza).

Supplementary materials

Supplementary material associated with this article can be found, in the online version, at doi:10.1016/j.actbio.2026.01.013.

References

[1] A. Ostman, M. Augsten, Cancer-associated fibroblasts and tumor growth–bystanders turning into key players, Curr. Opin. Genet. Dev. 19 (2009) 67–73.
[2] D.F. Quail, J.A. Joyce, Microenvironmental regulation of tumor progression and metastasis, Nat. Med. 19 (2013) 1423–1437.
[3] N.A. Bhowmick, A. Chytil, D. Plieth, A.E. Gorska, N. Dumont, S. Shappell, M. K. Washington, E.G. Neilson, H.L. Moses, TGF-beta signaling in fibroblasts modulates the oncogenic potential of adjacent epithelia, Science 1979 303 (2004) 848–851.
[4] S. Maman, I.P. Witz, A history of exploring cancer in context, Nat. Rev. Cancer 18 (2018) 359–376.
[5] K.C. Valkenburg, A.E. de Groot, K.J. Pienta, Targeting the tumour stroma to improve cancer therapy, Nat. Rev. Clin. Oncol. 15 (2018) 366–381.
[6] X. Zhang, T. Kim, T.J. Thauland, H. Li, F.S. Majedi, C. Ly, Z. Gu, M.J. Butte, A. C. Rowat, S. Li, Unraveling the mechanobiology of immune cells, Curr. Opin. Biotechnol. 66 (2020) 236–245.
[7] V. Gkretsi, T. Stylianopoulos, Cell adhesion and matrix stiffness: coordinating cancer Cell invasion and metastasis, Front. Oncol. 8 (2018) 145.
[8] K.R. Levental, H. Yu, L. Kass, J.N. Lakins, M. Egeblad, J.T. Erler, S.F.T. Fong, K. Csiszar, A. Giaccia, W. Weninger, M. Yamauchi, D.L. Gasser, V.M. Weaver, Matrix crosslinking forces tumor progression by enhancing integrin signaling, Cell 139 (2009) 891–906.
[9] R.K. Jain, Antiangiogenesis strategies revisited: from starving tumors to alleviating hypoxia, Cancer Cell 26 (2014) 605–622.
[10] P. Baluk, H. Hashizume, D.M. McDonald, Cellular abnormalities of blood vessels as targets in cancer, Curr. Opin. Genet. Dev. 15 (2005) 102–111.
[11] W. Wang, E.M. Lollis, F. Bordeleau, C.A. Reinhart-King, Matrix stiffness regulates vascular integrity through focal adhesion kinase activity, FASEB J. 33 (2019) 1199–1208.
[12] R.K. Jain, J.D. Martin, T. Stylianopoulos, The role of mechanical forces in tumor growth and therapy, Annu Rev. Biomed. Eng. 16 (2014) 321–346.
[13] H.T. Nia, L.L. Munn, R.K. Jain, Physical traits of cancer, Science 1979 370 (2020) eaaz0868, https://doi.org/10.1126/science.aaz0868.
[14] J.M. Northcott, I.S. Dean, J.K. Mouw, V.M. Weaver, Feeling stress: the mechanics of cancer progression and aggression, Front. Cell Dev. Biol. 6 (2018) 17.
[15] M. Bao, Y. Chen, J. Liu, H. Bao, W. Wang, Y. Qi, F. Lv, Extracellular matrix stiffness controls VEGF(165) secretion and neuroblastoma angiogenesis via the YAP/RUNX2/SRSF1 axis, Angiogenesis. 25 (2022) 71–86.
[16] B. Yi, Y. Shen, H. Tang, X. Wang, Y. Zhang, Stiffness of the aligned fibers affects structural and functional integrity of the oriented endothelial cells, Acta Biomater. 108 (2020) 237–249.
[17] M. Alamer, X.Y Xu, The influence of tumour vasculature on fluid flow in solid tumours: a mathematical modelling study, Biophys. Rep. 7 (2021) 35–54.
[18] Y. Navalitloha, E.S. Schwartz, E.N. Groothuis, C.V. Allen, R.M. Levy, D. R. Groothuis, Therapeutic implications of tumor interstitial fluid pressure in subcutaneous RG-2 tumors, Neuro Oncol. 8 (2006) 227–233.
[19] S. Ferretti, P.R. Allegrini, M.M. Becquet, P.M. McSheehy, Tumor interstitial fluid pressure as an early-response marker for anticancer therapeutics, Neoplasia 11 (2009) 874–881.
[20] T. Yang, H. Xiao, X. Liu, Z. Wang, Q. Zhang, N. Wei, X. Guo, Vascular normalization: a new window opened for cancer therapies, Front. Oncol. 11 (2021) 719836.
[21] K.A. Papavassiliou, E.K. Basdra, A.G. Papavassiliou, The emerging promise of tumour mechanobiology in cancer treatment, Eur. J. Cancer 190 (2023) 112938.
[22] T.C. Gasser, Vascular Biomechanics, Springer, 2021.
[23] C.M. Griffith, S.A. Huang, C. Cho, T.M. Khare, M. Rich, G. Lee, F.S. Ligler, B. O. Diekman, W.J. Polacheck, Microfluidics for the study of mechanotransduction, J. Phys. D. Appl. Phys. 53 (2020) 224004, https://doi.org/10.1088/1361-6463/ab78d4. Epub 2020 Apr 2.
[24] K.M. Chrobak, D.R. Potter, J. Tien, Formation of perfused, functional microvascular tubes in vitro, Microvasc. Res. 71 (2006) 185–196.

[25] V. Vickerman, R.D. Kamm, Mechanism of a flow-gated angiogenesis switch: early signaling events at cell-matrix and cell-cell junctions, Integr. Biol. 4 (2012) 863–874.

[26] S. Kim, M. Chung, J. Ahn, S. Lee, N.L. Jeon, Interstitial flow regulates the angiogenic response and phenotype of endothelial cells in a 3D culture model, Lab. Chip. 16 (2016) 4189–4199.

[27] Y. Liu, J. Zheng, L. Zhong, Z. Wang, D. Zhao, H. Lin, X. Zhang, K. Meng, X. Yang, D. Zhang, L. Lin, L. Qiao, Vessel-on-A-chip coupled proteomics reveal pressure-overload-induced vascular remodeling, Adv. Sci. (2025) 2415024 n/a.

[28] S.C. Neves, A. Sousa, D.S. Nascimento, I.D. Orge, S.A. Ferreira, C. Mota, L. Moroni, C.C. Barrias, P.L. Granja, A hybrid construct with tailored 3D structure for directing pre-vascularization in engineered tissues, Mater. Today Bio 29 (2024) 101291.

[29] E.L. Doherty, W.Y. Aw, A.J. Hickey, W.J. Polacheck, Microfluidic and organ-on-a-chip approaches to investigate cellular and microenvironmental contributions to cardiovascular function and pathology, Front. Bioeng. Biotechnol. 9 (2021) 624435.

[30] Y. Du, I.E.M. de Jong, K. Gupta, O. Waisbourd-Zinman, A. Har-Zahav, C.J. Soroka, J.L. Boyer, J. Llewellyn, C. Liu, A. Naji, W.J. Polacheck, R.G. Wells, Human vascularized bile duct-on-a chip: a multi-cellular micro-physiological system for studying cholestatic liver disease, Biofabrication. 16 (2023) 015004, https://doi.org/10.1088/1758-5090/ad0261.

[31] C. Franco, H. Gerhardt, Tissue engineering: blood vessels on a chip, Nature 488 (2012) 465–466.

[32] J. Song, J. Ko, N. Choi, N.L. Jeon, H.N. Kim, Tumor spheroid-based and microtumor-based vascularized models for replicating the vascularized tumor microenvironment, Organoid 3 (2023) e6.

[33] J. Ahn, D. Kim, D. Koo, J. Lim, T. Park, J. Lee, J. Ko, S. Kim, M. Kim, K. Kang, D. Min, S. Kim, Y. Kim, N.L. Jeon, 3D microengineered vascularized tumor spheroids for drug delivery and efficacy testing, Acta Biomater. 165 (2023) 153–167.

[34] S. Pérez-Rodríguez, S.A. Huang, C. Borau, J.M. García-Aznar, W.J. Polacheck, Microfluidic model of monocyte extravasation reveals the role of hemodynamics and subendothelial matrix mechanics in regulating endothelial integrity, Biomicrofluidics. 15 (2021) 054102.

[35] B. Parejo-Alonso, A. Royo-García, P. Espiau-Romera, S. Courtois, Á. Curiel-García, S. Zagorac, I. Villaoslada, K.P. Olive, C. Heeschen, P. Sancho, Pharmacological targeting of the receptor ALK inhibits tumorigenicity and overcomes chemoresistance in pancreatic ductal adenocarcinoma, Biomed. PharmacOther 158 (2023) 114162.

[36] F. Re, A. Zanetti, M. Sironi, N. Polentarutti, L. Lanfrancone, E. Dejana, F. Colotta, Inhibition of anchorage-dependent cell spreading triggers apoptosis in cultured human endothelial cells, J. Cell Biol. 127 (1994) 537–546.

[37] Y. Chen, X. Lou, Z. Zhang, P. Ingram, E. Yoon, High-throughput cancer cell sphere formation for characterizing the efficacy of photo dynamic therapy in 3D cell cultures, Sci. Rep. 5 (2015) 12175.

[38] W.J. Polacheck, M.L. Kutys, J.B. Tefft, C.S. Chen, Microfabricated blood vessels for modeling the vascular transport barrier, Nat. Protoc. 14 (2019) 1425–1454.

[39] S. Hernández-Hatibi, P.E. Guerrero, J.M. García-Aznar, E. García-Gareta, Polydopamine interfacial coating for stable tumor-on-a-chip models: application for pancreatic ductal adenocarcinoma, Biomacromolecules. 25 (2024) 5169–5180.

[40] I.D. Orge, H.N. Pinto, M.A. Silva, S.J. Bidarra, S.A. Ferreira, I. Calejo, R. Masereeuw, S.M. Mihăilă, C.C. Barrias, Vascular units as advanced living materials for bottom-up engineering of perfusable 3D microvascular networks, Bioact. Mater. 38 (2024) 499–511.

[41] C.A. Dessalles, C. Ramón-Lozano, A. Babataheri, A.I. Barakat, Luminal flow actuation generates coupled shear and strain in a microvessel-on-chip, Biofabrication. 14 (2021), https://doi.org/10.1088/1758-5090/ac2baa.

[42] J. Schindelin, I. Arganda-Carreras, E. Frise, V. Kaynig, M. Longair, T. Pietzsch, S. Preibisch, C. Rueden, S. Saalfeld, B. Schmid, J. Tinevez, D.J. White, V. Hartenstein, K. Eliceiri, P. Tomancak, A. Cardona, Fiji: an open-source platform for biological-image analysis, Nat. Methods 9 (2012) 676–682.

[43] C. Stringer, T. Wang, M. Michaelos, M. Pachitariu, Cellpose: a generalist algorithm for cellular segmentation, Nat. Methods 18 (2021) 100–106.

[44] A.R. Henderson, I.S. Ilan, E. Lee, A bioengineered lymphatic vessel model for studying lymphatic endothelial cell-cell junction and barrier function, Microcirculation. 28 (2021) e12730.

[45] A.M.N. Walker, N. Warmke, B. Mercer, N.T. Watt, R. Mughal, J. Smith, S. Galloway, N.J. Haywood, T. Soomro, K.J. Griffin, S.B. Wheatcroft, N. Y. Yuldasheva, D.J. Beech, P. Carmeliet, M.T. Kearney, R.M. Cubbon, Endothelial insulin receptors promote VEGF-A signaling via ERK1/2 and sprouting angiogenesis, Endocrinology 162 (2021) bqab104.

[46] A. Sedlář, M. Trávníčková, R. Matějka, Š. Pražák, Z. Mészáros, P. Bojarová, L. Bačáková, V. Křen, K. Slámová, Growth factors VEGF-A165 and FGF-2 as multifunctional biomolecules governing cell adhesion and proliferation, Int. J. Mol. Sci. 22 (2021).

[47] M. Milacic, D. Beavers, P. Conley, C. Gong, M. Gillespie, J. Griss, R. Haw, B. Jassal, L. Matthews, B. May, R. Petryszak, E. Ragueneau, K. Rothfels, C. Sevilla, V. Shamovsky, R. Stephan, K. Tiwari, T. Varusai, J. Weiser, A. Wright, G. Wu, L. Stein, H. Hermjakob, P. D'Eustachio, The reactome pathway knowledgebase 2024, Nucleic. Acids. Res. 52 (2024) D672–D678.

[48] M. Kalli, T. Stylianopoulos, Defining the role of solid stress and matrix stiffness in, Cancer Cell Prolif. Metastasis Front. Oncol. 8 (2018) 55.

[49] P.J. Critser, S.T. Kreger, S.L. Voytik-Harbin, M.C. Yoder, Collagen matrix physical properties modulate endothelial colony forming cell-derived vessels in vivo, Microvasc. Res. 80 (2010) 23–30.

[50] A.L. Sieminski, R.P. Hebbel, K.J. Gooch, The relative magnitudes of endothelial force generation and matrix stiffness modulate capillary morphogenesis in vitro, Exp. Cell Res. 297 (2004) 574–584.

[51] S. Barrasa-Ramos, C.A. Dessalles, M. Hautefeuille, A.I. Barakat, Mechanical regulation of the early stages of angiogenesis, J. R. Soc. Interface 19 (2022) 20220360.

[52] A.V. Nguyen, B. Trompetto, X.H.M. Tan, M.B. Scott, K.H. Hu, E. Deeds, M.J. Butte, P.Y. Chiou, A.C. Rowat, Differential contributions of actin and myosin to the physical phenotypes and invasion of pancreatic cancer cells, Cell Mol. Bioeng. 13 (2020) 27–44.

[53] D. Kpeglo, M.D.G. Hughes, L. Dougan, M. Haddrick, M.A. Knowles, S.D. Evans, S. A. Peyman, Modeling the mechanical stiffness of pancreatic ductal adenocarcinoma, Matrix. Biol. Plus. 14 (2022) 100109.

[54] D. Zhao, C. Xue, Q. Li, M. Liu, W. Ma, T. Zhou, Y. Lin, Substrate stiffness regulated migration and angiogenesis potential of A549 cells and HUVECs, J. Cell Physiol. 233 (2018) 3407–3417.

[55] B. Patra, M. Sharma, W. Hale, M. Utz, Time-resolved non-invasive metabolomic monitoring of a single cancer spheroid by microfluidic NMR, Sci. Rep. 11 (2021) 1–53.

[56] M.M. Schroll, X. Liu, S.K. Herzog, S.B. Skube, A.B. Hummon, Nutrient restriction of glucose or serum results in similar proteomic expression changes in 3D colon cancer cell cultures, Nutr. Res. 36 (2016) 1068–1080.

[57] P. Guerrero-López, A. Martín-Pardillos, J. Bonet-Aleta, A. Mosseri, J.L. Hueso, J. Santamaria, J. Garcia-Aznar, 2D versus 3D tumor-on-chip models to study the impact of tumor organization on metabolic patterns in vitro, Sci. Rep. 15 (2025) 19506.

[58] S. Hernández-Hatibi, C. Borau, N. Martínez-Bosch, P. Navarro, J.M. García-Aznar, P.E. Guerrero, Quantitative characterization of the 3D self-organization of PDAC tumor spheroids reveals cell type and matrix dependence through advanced microscopy analysis, APL. Bioeng. 9 (2025) 016116.

[59] R. Krishnan, D.D. Klumpers, C.Y. Park, K. Rajendran, X. Trepat, J. van Bezu, V.W. M. van Hinsbergh, C.V. Carman, J.D. Brain, J.J. Fredberg, J.P. Butler, G.P. van Nieuw Amerongen, Substrate stiffening promotes endothelial monolayer disruption through enhanced physical forces, Am. J. Physiol.-Cell Physiol. 300 (2011) C146–C154.

[60] P. DEMBÉLÉ, O. GARNIER, D.K. MARTIN, I. VILGRAIN, Microtumor spheroids provide a model for studying molecules involved in vascular organization: an illustrative study for VE-cadherin, Anticancer Res. 42 (2022) 4689–4700.

[61] M.S. Singh, M. Goldsmith, K. Thakur, S. Chatterjee, D. Landesman-Milo, T. Levy, L. A. Kunz-Schughart, Y. Barenholz, D. Peer, An ovarian spheroid based tumor model that represents vascularized tumors and enables the investigation of nanomedicine therapeutics, Nanoscale 12 (2020) 1894–1903.

[62] N. Klusmeier, H. Schnittler, J. Seebach, A novel microscopic assay reveals heterogeneous regulation of local endothelial barrier function, Biophys. J. 116 (2019) 1547–1559.

[63] C. Valero, H. Amaveda, M. Mora, J.M. García-Aznar, Combined experimental and computational characterization of crosslinked collagen-based hydrogels, PLoS. One 13 (2018) e0195820.

[64] H.T. Nia, L.L. Munn, R.K. Jain, Physical traits of cancer, Science 1979 370 (2020) eaaz0868.

[65] D.J.V. David, Responses to stiffening, Nat. Cell Biol. 27 (2025) 1201.

[66] K. Kane, D. Edwards, J. Chen, The influence of endothelial metabolic reprogramming on the tumor microenvironment, Oncogene 44 (2025) 51–63.

[67] S.W.S. Leung, Y. Shi, The glycolytic process in endothelial cells and its implications, Acta Pharmacol. Sin. 43 (2022) 251–259.

[68] B. Liu, Z. Dai, Fatty acid metabolism in endothelial cell, Genes 13 (2022) 2301, https://doi.org/10.3390/genes13122301.

[69] H. Huang, S. Vandekeere, J. Kalucka, L. Bierhansl, A. Zecchin, U. Brüning, A. Visnagri, N. Yuldasheva, J. Goveia, B. Cruys, K. Brepoels, S. Wyns, S. Rayport, B. Ghesquière, S. Vinckier, L. Schoonjans, R. Cubbon, M. Dewerchin, G. Eelen, P. Carmeliet, Role of glutamine and interlinked asparagine metabolism in vessel formation, EMBO J. 36 (2017) 2334–2352.

[70] E.O. Gómez, Y.I. Chirino, N.L. Delgado-Buenrostro, A. López-Saavedra, N. Meraz-Cruz, R. López-Marure, Secretome derived from breast tumor cell lines alters the morphology of human umbilical vein endothelial cells, Mol. Membr. Biol. 33 (2016) 29–37.

[71] C. Bourreau, E. Navarro, M. Cotinat, M. Krejbich, F. Guillonneau, C. Guette, A. Boissard, C. Henry, I. Corre, L. Treps, N. Clere, Secretomes from non-small cell lung cancer cells induce endothelial plasticity through a partial endothelial-to-mesenchymal transition, Cancer Med. 14 (2025) e70707.

[72] H. Cheng, Y. Chen, J. Wong, C. Weng, H. Chen, S. Yu, H. Chen, A. Yuan, J.J. W. Chen, Cancer cells increase endothelial cell tube formation and survival by activating the PI3K/akt signalling pathway, J. Exp. Clin. Cancer Res. 36 (2017) 27.